Applied Catalysis B: Environmental 198 (2016) 295–302

Contents lists available at ScienceDirect

Applied Catalysis B: Environmental

journal homepage: www.elsevier.com/locate/apcatb

Activation of peroxymonosulfate by carbonaceous oxygen groups: experimental and density functional theory calculations

Yuxian Wang[a,b], Zhimin Ao[c], Hongqi Sun[d,*], Xiaoguang Duan[a], Shaobin Wang[b,*]

[a] State Key Laboratory of Heavy Oil Processing, China University of Petroleum, Beijing, 18 Fuxue Road, Beijing, 102249, PR China
[b] Department of Chemical Engineering, Curtin University, GPO Box U1987, Perth, Western Australia, 6845, Australia
[c] Institute of Environmental Health and Pollution Control, School of Environmental Science and Engineering, Guangdong University of Technology, Guangzhou, 510006, PR China
[d] School of Engineering, Edith Cowan University, 270 Joondalup Drive, Joondalup, Western Australia 6027, Australia

ARTICLE INFO

Article history:
Received 19 April 2016
Received in revised form 28 May 2016
Accepted 30 May 2016
Available online 31 May 2016

Keywords:
Active sites
Sulfate radicals
Carbon spheres
DFT
Catalytic oxidation

ABSTRACT

The active sites for metal-free carbocatalysis in environmental remediation are intricate compared to those for traditional metal-based catalysis. In this study, we report a facile fabrication of amorphous carbon spheres with varying oxygen functional groups by hydrothermal treatment of glucose solutions. With air/N_2 annealing and regeneration in the glucose solution of the as-synthesized carbon spheres, the concentrations of oxygen-containing groups were tailored on the amorphous carbon spheres in an Excess-On-Off-On manner. Accordingly, an Off-On-Off-On catalytic behavior in peroxymonosulfate (PMS) activation using these amorphous carbon spheres was observed. To uncover the mechanism of catalytic activity, electron spin resonance (EPR) spectra were recorded to investigate the variation of the generated $^{\bullet}OH$ and $SO_4^{\bullet-}$ radicals. Moreover, density functional theory (DFT) studies were employed to identify the role of oxygen-containing groups on the amorphous carbon spheres in adsorptive O—O bond activation of PMS. Results revealed that ketone groups (C═O) are the dominant active sites for PMS activation among oxygen-containing functional groups. In order to simulate real wastewater treatment, influences of chloride anions and humic acid on PMS activation for phenol degradation were further evaluated. This study provides an in-depth insight to discovering the role of oxygen-containing functional groups as the active sites in metal-free carbocatalysis.

1. Introduction

With the rapid development of industrialization and urbanization, environmental deterioration, especially water resource depletion, has posed great public concerns for pivoting this resources-lack world to a sustainable future. In the past years, considerable research efforts have been dedicated to water resource remediation, including physical adsorption, bio-degradation, membrane separation, chemical oxidation and flocculation [1–3]. However, most of these technologies are cost/energy intensive with incomplete remediation capabilities and/or low purification efficiencies, leading to further treatment still required [4]. In recent years, advanced oxidation processes (AOPs) utilizing reactive species have displayed their promising capabilities in effective water remediation owing to excellent degradation efficiency and complete mineralization of the toxic organic pollutants [5–7].

Among AOPs, peroxymonosulfate (PMS, commercially known as Oxone®) has become a favorable alternative to hydrogen peroxide (H_2O_2) for environmental catalysis to overcome the drawbacks of Fenton reactions, such as a low pH range, large amounts of sludge generation and cost-intensive storage and transportation of the oxidant [8,9]. Due to the high redox potentials, the produced sulfate radicals ($E_0 \approx 3.1$ V) and hydroxyl radicals ($E_0 \approx 2.7$ V) from PMS activation are responsible for non-selective oxidation of harmful organic compounds [10]. Homogenous PMS activation using Co(II), Mn(II), Fe(II), Ru(III), and Ag(I) ions [10–12] or heterogeneous activation by cobalt oxides [13], manganese oxides [14,15], or supported metal catalysts [16,17] demonstrated a superb degradation efficiency because of the variable chemical states and unoccupied orbitals of these metal-based catalysts, yet they experienced severe metal leaching which results in secondary contamination to water body [18]. Therefore, metal-free catalysis was recently suggested to be a green process for water remediation [19,20].

* Corresponding authors.
E-mail addresses: h.sun@ecu.edu.au (H. Sun), shaobin.wang@curtin.edu.au, shaobin.wang@exchange.curtin.edu.au (S. Wang).

http://dx.doi.org/10.1016/j.apcatb.2016.05.075
0926-3373/

In terms of carbocatalysis, carbon-based materials such as graphene oxide (GO), graphene, carbon nanotubes (CNTs), and activated carbon have been demonstrated to be catalytically effective for energy and environmental applications [21–24]. In previous studies, we applied for the first time such carbon catalysts for heterogeneous PMS activation for decomposition of aqueous organic pollutants [25–27]. Chemically reduced graphene oxide (rGO) was firstly discovered for PMS activation to produce reactive radicals for decomposition of various organics in water [25]. With the rGO, sp^2 hybridized carbon, oxygen-containing functional groups and edge defects (zigzag or armchair) were suggested to be the catalytic active sites [25,28]. In a subsequent study [27], nitrogen doped rGO with chemically modified sp^2 carbon showed enhanced catalysis due to the N heteroatoms at defective sites, which demonstrated the contributions of both defective sites and nitrogen dopant to the catalytic activity. Then multiwall carbon nanotubes (MWCNTs) with minimized structural defects and oxygen functional groups were also tested for PMS activation [26]. However, in the above studies, a variety of active sites on nanocarbons were involved in PMS activation, due to the chemical nature of rGO or carbon nanotubes, such as sp^2 carbon, defective structure and oxygen-containing groups. The contribution of different types of active sites to the carbocatalysis is still not clear and conclusive. Moreover, to the best of our knowledge, there is no research focusing on switching on/off the catalytic activity of carbocatalysts by manipulating the specific active sites in environmental remediation.

It was suggested that amorphous carbon with oxygen functional groups can be obtained by hydrothermal carbonization of carbohydrates [29]. In this study, amorphous carbon spheres were fabricated via a facile one-step hydrothermal method (**Excess** mode). By such an elaborate design, we ruled out the contribution of sp^2 hybridized carbon atoms and edge defects to the catalytic activity (as well as doped nitrogen), and exclusively focused on oxygen-containing groups. Meanwhile, concentrations of the surface oxygen-functional groups were successfully manipulated by air annealing (**On**^{1} mode), N_2 annealing (**Off** mode) and regeneration in a glucose solution (**On**^{2} mode). We evaluated the contribution of oxygen functional groups to PMS activation by testing the catalytic activities of these amorphous carbon spheres with different modes toward phenol degradation. Moreover, to provide theoretically insights into the role of oxygen functional groups on the carbons in catalysis, we further employed density functional theory (DFT) calculations by constructing molecular amorphous carbon models containing —OH, —C═O, —COOH and three adjacent —C═O groups. We dedicate this research to developing novel green catalysts for environmental remediation and revealing the contribution of oxygen functional groups to carbocatalysis.

2. Experimental

2.1. Materials and chemicals

D-glucose (99.8%) and Oxone® ($2KHSO_5{\cdot}KHSO_4{\cdot}K_2SO_4$, PMS) were obtained from Sigma-Aldrich. Phenol (99.8%) was purchased from Ajax Finechem. 5,5- Dimethyl- 1- pyrroline (DMPO, >99.0%) was obtained from Fluka. Multi-walled carbon nanotubes (MWCNTs, >99.5%) were purchased from Chengdu Organic Chemical, China. All chemicals were used as received without further purification.

2.2. Preparation of carbon materials

Fresh carbon nanospheres (CS, **Excess** model of oxygen groups) were prepared by hydrothermal carbonization of glucose at 180 °C for 18 h. For tailoring the oxygen-functional groups, CS-AIR (**On**^{1} model of oxygen groups) was prepared by annealing the CS in air at 350 °C for 1 h; CS-N_2 (**Off** model of oxygen groups) was fabricated by annealing the CS in nitrogen 400 °C for 1 h; and CS-REG (**On**^{2} model of oxygen groups) was obtained by hydrothermal treatment of CS-N_2 in a glucose solution at 180 °C for 3 h. Detailed synthesis routes for tailoring oxygen-functional groups could be found in the Supplementary Data.

2.3. Characterization

Structure and morphology of the materials were observed on a ZEISS NEON 40EsB scanning electron microscope (SEM). XRD (X-ray diffraction) patterns were performed on a Bruker D8 diffractometer (Bruker-AXS, Karlsruhe, Germany) using filtered Cu Kα radiation (λ = 1.5418 Å) with an accelerating voltage of 40 kV and a current of 30 mA. The Brunauer–Emmett–Teller (BET) specific surface area and the pore size distribution of the samples were measured by N_2 adsorption/desorption using a Micromeritics Tristar 3000. Prior to measurement, the samples were degassed at 150 °C overnight under vacuum condition. Fourier transform infrared spectra (FTIR) were obtained from a Bruker instrument with an ATR correction mode. Raman study was measured on an ISA dispersive Raman spectrometer using argon ion lasers (514 nm). X-ray photoelectron microscopy (XPS) was acquired on a Kratos AXIS Ultra DLD system under UHV condition with Al-Kα X-ray. Spectra were fitted with Kratos Vision and CasaXPS software.

2.4. PMS activation and catalytic oxidation

The catalytic oxidation of phenol was carried out in a 500 mL conical flask containing 20 ppm of phenol solution with a constant stirring at 300 rpm. The reactor was attached to a stand and dipped into a water bath with a temperature controller. Unless specifically stated, the reaction temperature was maintained at 25 °C. In a typical test, 0.1 g catalyst was firstly added into the phenol solution for 30 min to achieve adsorption-desorption equilibrium, and then 2 g/L PMS was added into the solution. At certain intervals, 1 mL aqueous sample was withdrawn by a syringe and filtered into a HPLC vial, which was prior injected by 0.5 mL of methanol to quench the reaction. The concentration of phenol was analyzed using a Varian HPLC with a UV detector at wavelength of 270 nm. A C-18 column was used to separate the organics while the mobile phase with a flow rate of 1 mL/min was made of 30% CH_3CN and 70% water. Total organic carbon (TOC) was measured on a Shimadzu TOC-vcph analyzer at fixed time intervals during the reaction. For the recycle tests of the catalyst, after each run, the catalyst was obtained by vacuum filtration and washed with ultrapure water for 3 times. Then the washed catalyst was dried in an oven at 60 °C for 12 h. For catalytic phenol degradation, experiments were repeated three times in order to obtain error bars on the plots. The electron paramagnetic resonance (EPR) from a Bruker EMS-plus was employed to detect the radicals generated during activation of PMS, operating at following conditions: center field: 3517 G; sweep width: 100 G; sweep time 30 s; microwave frequency: 9.87 GHz; power setting: 18.75 mW.

2.5. Computational models and methodology

The spin-polarized density functional theory (DFT) calculations in this work were executed using the DMOL^3 module [30]. The local density approximation (LDA) with Perdew-Wang correlation (PWC) function was utilized as the exchange-correlation function. A double numerical plus polarization (DNP) was used as the basis set, while the All Electron core treatment was utilized to include relativistic effects. The convergence tolerance of the energy was set to 10^{-5} Ha (1 Ha = 27.21 eV), and the maximum allowed force

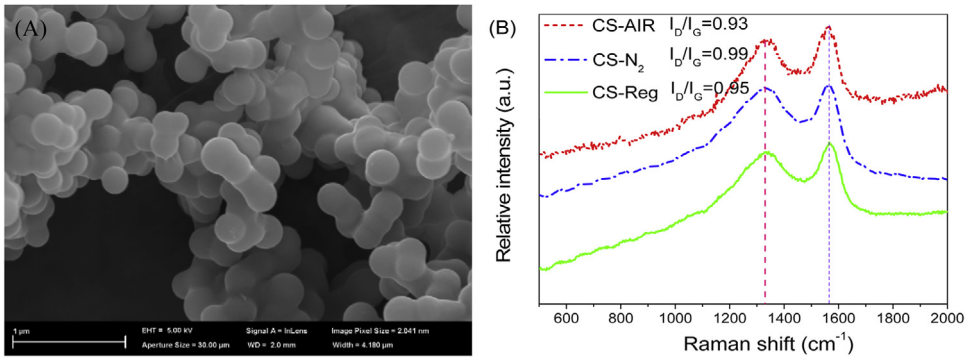

Fig. 1. (A) SEM image of CS-AIR, (B) Raman spectra of CS samples.

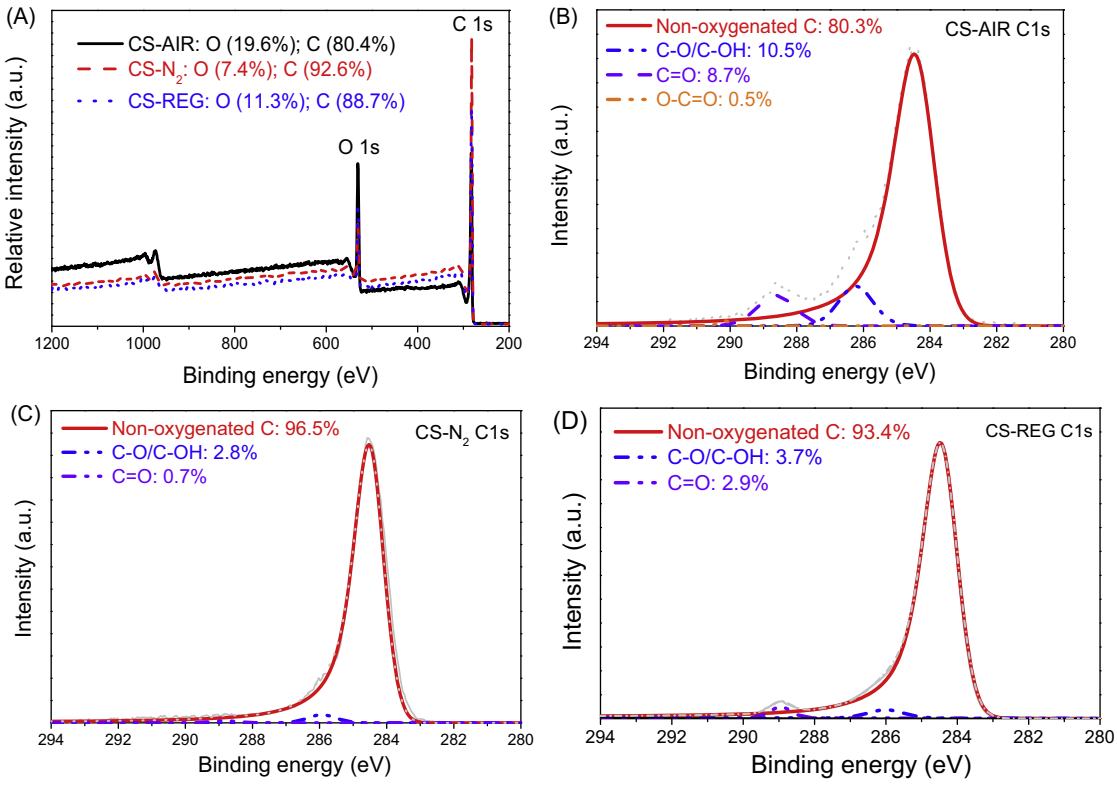

Fig. 2. (A) XPS survey of CS samples; (B) HR XPS spectra of C 1 s region of CS-AIR; (C) HR XPS spectra of C 1 s region of CS-N_2; (D) HR XPS spectra of C 1 s region of CS-REG.

and displacement were 0.002 Ha/Å and 0.005 Å, respectively. In the calculation, a cluster model was used and all the atoms are allowed to relax. The DFT-D correction with OBS method was used in all calculations to consider the van der Waals forces [31]. The minimum energy of each system was set as the basis energy.

3. Results and discussion

The morphology of CS-AIR was displayed in Fig. 1(A). A spherical morphology of CS-AIR was observed with significant aggregation of uniformed spheres with an average size of 300–350 nm. SEM images of CS-N_2 and CS-REG shown in Fig. S1 indicate that the various treatments did not affect the morphology of the samples. For CS with different treatments, characteristic D-band (1349 cm^{-1}) and G-band (1569 cm^{-1}) were observed in Raman spectra (Fig. 1(B)), consistent with those amorphous carbon reported [32]. The high I_D/I_G ratio with broad bands revealed the poor crystallinity of the samples [33]. Meanwhile, an infinitesimal variation of I_G/I_D ratio occurred to the three CS samples, suggesting that the amorphous structure of the CS samples was barely affected by different treatments. XRD patterns of CS samples are shown in Fig. S2. No discernible peaks were observed, indicating neither sp^2 carbon nor graphite was produced, thus confirming the amorphous structure of these carbon spheres.

Full XPS survey in Fig. 2(A) indicates the compositional information of the tailored carbon spheres. Fig. 2(B) shows CS-AIR has strong signals at 286.2 and 288.6 eV, suggesting that most of the oxygen-containing groups on CS-AIR were in the forms of C—OH (10.52 at.%) and C=O (8.7 at.%). This confirms the formation of On^1–model. While for CS-N_2, C 1 s XPS spectrum (Fig. 2(C)) suggests a dramatic decrease in carbon-bonded oxygen groups. Particularly, C=O group decreases from 8.7 at.% to 0.7 at.%. The low concentration of the oxygen containing groups reveals that CS-N_2 has very limited oxygen-containing functional groups on its surface due to the N_2 annealing, leading to the Off-model. The recovery of oxygen containing groups can be achieved by glucose retreatment. Compared with CS-N_2, the concentrations of C—OH and C=O groups on CS-REG

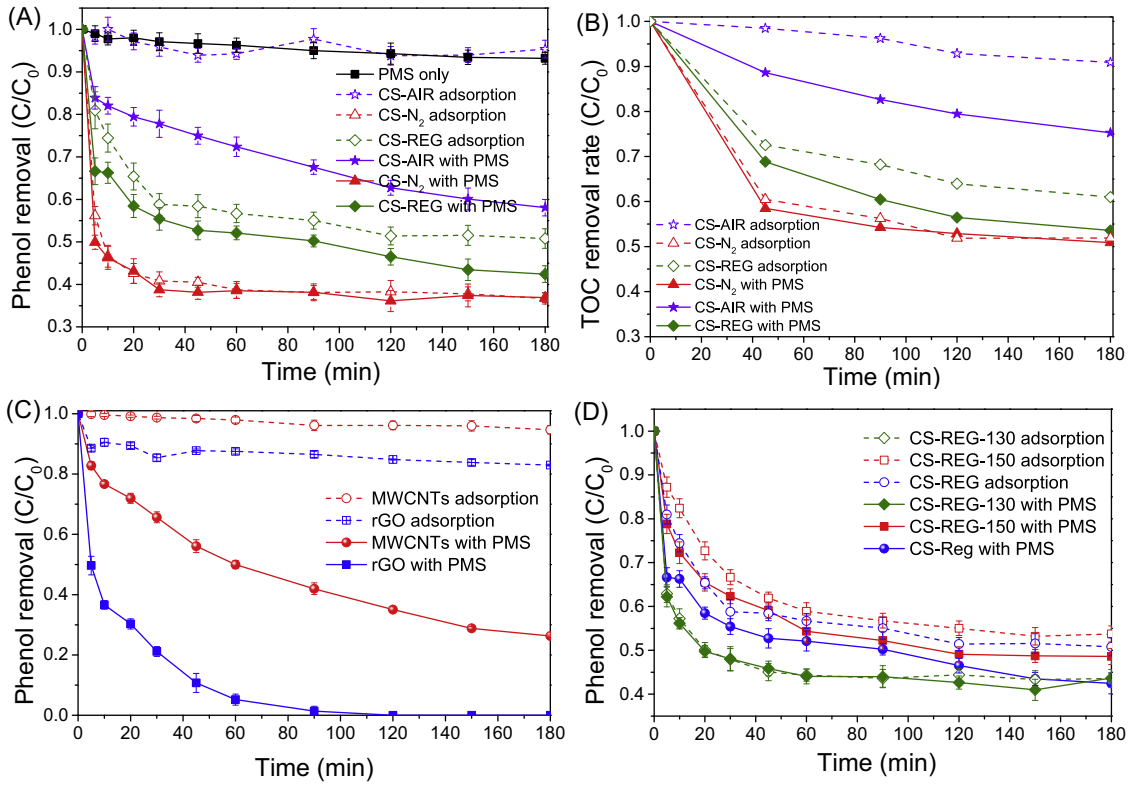

Fig. 3. (A) Catalytic oxidation of phenol on different CS samples; (B) TOC removal efficiency of CS-AIR, CS-N_2 and CS-REG; (C) Catalytic oxidation on rGO and MWCNTs; and (D) Catalytic oxidation on CS-REG prepared at different temperatures. $[Phenol]_0$ = 20 mg/L; catalyst loading = 0.2 g/L; [PMS] = 2 g/L; Temperature: 25 °C.

Table 1
Textural properties of carbon spheres treated with different methods.

Sample	Surface area (S_{BET} m^2/g)	Pore volume (cm^3/g)	Average pore diameter (nm)
CS-AIR	383	0.021	0.41
CS-N_2	296	0.017	0.54
CS-REG	196	0.012	0.52

increase to 3.7 and 2.9 at.%, respectively. And the XPS spectra of the CS samples on O 1 s further validate the changes of oxygen containing groups (Fig.S3). This suggests the generation of On^2–model. XPS results indicate that, by tuned with various methods, the proportion of oxygen-contained groups especially the proportion of O═C group varied and the order is CS-AIR (On^1-model) > CS-REG (On^2-model) > CS-N_2 (Off-model).

Fig. S4 displays FTIR spectra of CS samples. The bands centered at 2889, 1730, 1602 and 1286 cm^{-1} were observed for all samples, corresponding to C—H group, C═O group/C═C group and C—OH/C—O stretching and OH bending vibration, respectively [33,34]. The broad peaks at around 3500 cm^{-1} could be assigned to O—H stretching vibration [35]. It was also found that C═O peak intensity follows the order of CS-AIR > CS-REG > CS-N_2. The level variation of the functional groups was also reflected in their BET surface areas (Fig. S5 and Table 1). CS-AIR obtained the S_{BET} of 383 m^2/g, larger than CS-N_2 (296 m^2/g), indicating that thermal treatment in air enabled the CS to be more porous than N_2 annealing. It is noteworthy that CS-REG presented a lower S_{BET} (196 m^2/g) than CS-N_2. Considering the effect of glucose treatment, the decrease of the surface area would be due to the regrowth of functional groups on the surface of CS. While the pore size distributions revealed that the three amorphous carbon sphere samples possessed a similar pore size at around 0.5 nm.

The adsorptive and catalytic performances of these carbon spheres were examined by phenol removal as shown in Fig. 3 (A). PMS could hardly degrade phenol without a catalyst. While for adsorption tests, CS-AIR, CS-N_2 and CS-REG provided 5%, 60% and 45% phenol removal, respectively. Interestingly, the adsorption capabilities of these carbon spheres are not closely related with their S_{BET} order (Table 1). The differences in adsorption capabilities might be attributed to the surface functional groups. Since most of oxygen-containing functional groups were removed under N_2 treatment, the surface of the carbon spheres became more hydrophobic which is favorable for phenol adsorption. While the recovery of functional groups by glucose retreatment brought about a decrease in phenol adsorption. For catalytic oxidation via PMS activation, by deducting their corresponding adsorption contributions, 35% and 10% extra phenol removals were achieved on CS-AIR (On^1–model) and CS-REG (On^2–model) activation of PMS, respectively. While CS-N_2 (Off-model) could barely achieve phenol removal, and catalytic degradation profile overlapped the adsorption. The corresponding TOC removal efficiencies using the three catalysts were displayed in Fig. 3(B). Similar to phenol removal results, without the presence of PMS, CS-AIR demonstrated insignificant TOC removal capability. However, when PMS was involved, around 30% of TOC was mineralized and manifested a distinct margin against the adsorption. For CS-N_2 (Off model), it could be observed that, though it presented the highest TOC removal, the TOC removal profiles for adsorption and catalytic degradation almost overlapped, confirming the negligible catalytic activity under "Off model". For CS-REG, TOC removal rate for adsorption and catalytic degradation was 35% and 40%, respectively, indicating the recovery of the catalytic activity after glucose regeneration.

Catalytic activities of CS samples were still not in the order of S_{BET}, indicating surface area was not the key factor governing the catalysis. It was reported that active sites for nanocarbon materials are closely related to the intricate electronic states and

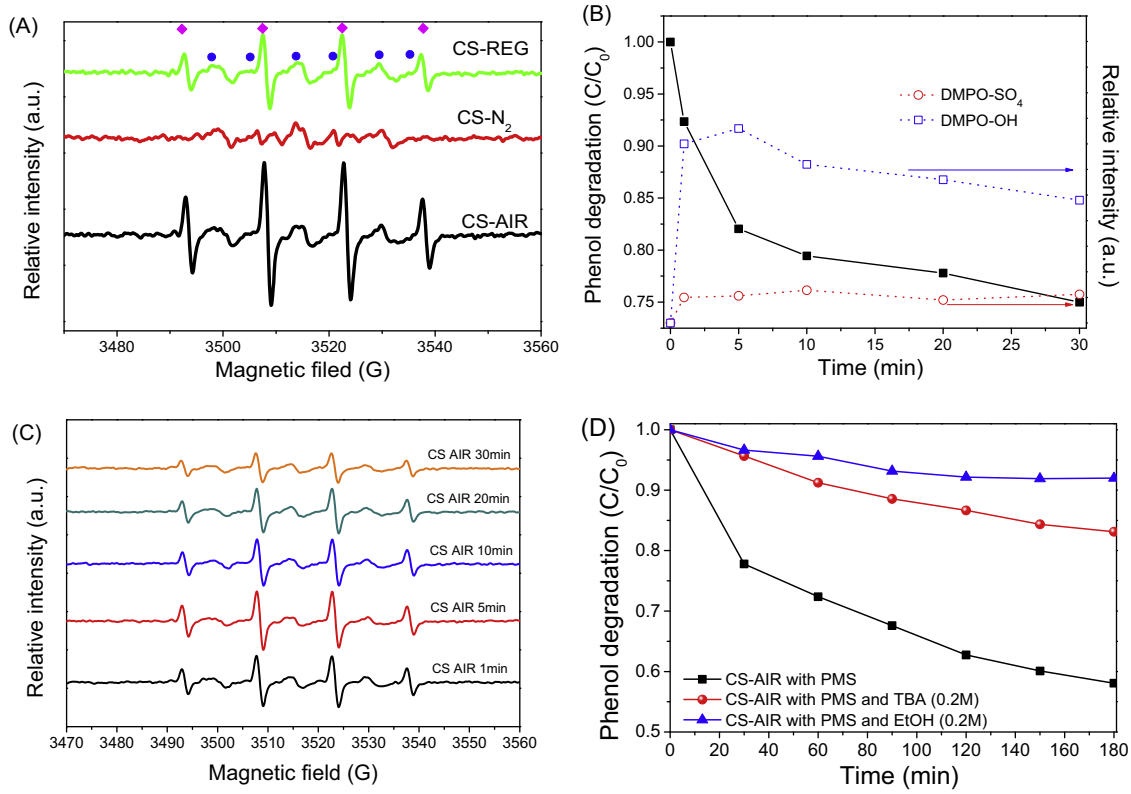

Fig. 4. (A) EPR spectra of PMS activation (♦: DMPO—OH, ●: DMPO-SO_4); (B) Radical evolution during PMS activation on CS-AIR; (C) EPR spectra at different reaction time; (D) Competitive radical tests using TBA (0.2 M) or EtOH (0.2 M) as a scavenger. $[Phenol]_0$ = 20 mg/L; catalyst loading = 0.2 g/L; [PMS] = 2 g/L; temperature: 25 °C; DMPO: 0.08 M.

spin feature of the covalent carbon system [36]. Previous studies suggested that the sp^2 hybridized structure obtaining abundant free-flowing electrons, the oxygen-containing functional groups with rich electrons, and the defective sites such as zigzag edges with delocalized π electrons are possibly the active sites in catalytic reactions [23,25,37,38]. To provide a thorough evaluation of these possible active sites, the catalytic activities of rGO (made by thermal exfoliation of GO) and pristine MWCNTs for PMS activation were investigated as the comparison (Fig. 3(C)). As seen, rGO had an excellent catalytic activity by possessing sp^2 structure, defective sites and functional groups. And the synergistic effect of these active sites enabled complete phenol removal to be achieved within 120 min. For pristine MWCNTs consisting of sp^2 structure and very limited functional groups, the catalytic activity decreased and 70% phenol removal was achieved in 3 h.

The amorphous carbon spheres synthesized in this work successfully ruled out both sp^2 hybridized structure and defective sites, yet still demonstrated to be catalytically active. Moreover, with different tuning strategies, the manipulation of the proportion of surface oxygen-containing functional groups (especially the C=O groups) was achieved. Moreover, the carbon spheres with different proportions of surface oxygen-containing functional groups demonstrated significant divergence in catalytic activities. A general trend was observed that carbon sphere with a higher C=O concentration provided a better catalytic performance. CS-AIR (On^1–model) obtaining the highest C=O concentration (8.7 at.%) has the best catalytic activity. When CS-AIR was annealed in N_2 (Off-model), C=O concentration dramatically decreased to 0.67 at.%, leading to negligible catalytic activity. However, the catalyst regained its activity when further treated with a glucose solution under hydrothermal condition (On^2–model) and the corresponding proportion of C=O group was elevated to 2.9 at.%. Fig. 3(D) further shows the influence of the retreated hydrothermal temperature. As seen, CS-REG at higher hydrothermal temperature obtained lower adsorption ability but better catalytic performance, revealing more oxygen-containing functional groups resulted from glucose dehydrating condensation regrew on the carbon spheres at elevated temperature. And the evolution of the reaction intermediates for glucose dehydrating condensation under different hydrothermal temperatures was illustrated by mass spectroscopy (MS) in Fig. S6 (SI).

Carbocatalysis on the samples was further investigated by electron paramagnetic resonance (EPR) using 5,5-dimethyl-1-pyrroline N-oxide (DMPO) as a radical spin trapping agent (Fig. 4 (A)). Spin trapping adducts DMPO—OH ($\alpha_H = \alpha_N = 14.8$) and DMPO—$SO_4$ ($\alpha_H = 0.78$, $\alpha_H = 1.48$, $\alpha_H = 9.6$, and $\alpha_N = 13.2$) were identified when CS-AIR (On^1-model) was employed as the catalyst, suggesting that CS-AIR could effectively activate PMS to generate hydroxyl and sulfate radicals responsible for phenol degradation [39]. For CS-N_2 (Off-model), very weak signals were observed for both hydroxyl and sulfate radicals, revealing insignificant activation, which was well in agreement with catalytic oxidation. After glucose treatment, EPR spectrum with discernible hydroxyl and sulfate radical peaks was observed for CS-REG (On^2-model), indicating that catalytic activity was regained. It is noteworthy that the lower peak intensity of the radicals from CS-REG (On^2-model) than CS-AIR (On^1-model) suggested an inferior catalytic activity. Previous study discovered that *p*-benzoquinone (*p*-BQ) could activate PMS to produce reactive species for pollutants degradation and the ketone groups were proved as the active sites [40]. Moreover, our recent study also observed the hydroxyl and sulfate radicals' EPR characteristic spectra when *p*-BQ was employed as the homogeneous catalysts for PS activation, which further consolidates the effect of ketone groups as the active sites in carbocatalysis [41].

Fig. 4(B) displays the variation of hydroxyl radical and sulfate radical intensities during the catalytic reaction. In this study, large

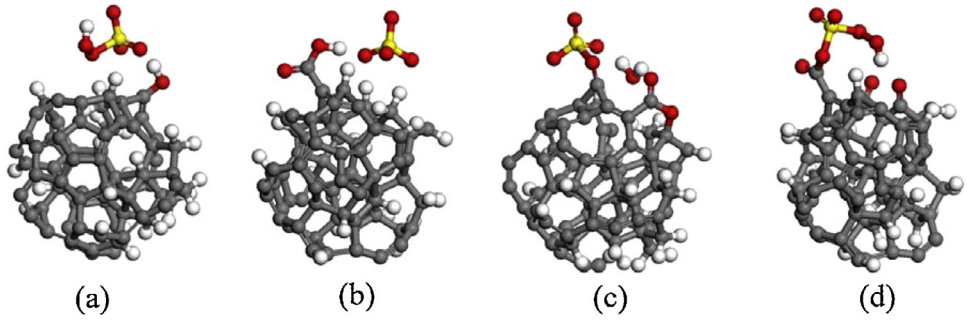

Scheme 1. CS models with different oxygen-containing functional groups for PMS adsorption. The C, H, O, and S atoms are represented in grey, white, red, and yellow, respectively. (a) CS with —OH group only; (b) CS with —C=O only; (c) CS with —COOH group only; and (d) CS with three adjacent —C=O groups. (For interpretation of the references to colour in this figure legend, the reader is referred to the web version of this article.)

quantity of hydroxyl radicals were produced at first 5 min, and then the amounts decreased gradually to a relatively steady level. The same scenario also occurred to sulfate radicals with a lower intensity. The C=O group on CS-AIR surface could activate PMS to produce both hydroxyl and sulfate radicals. Due to the high redox potential, hydroxyl and sulfate radicals would react with phenol quickly and thus leading to the decrease in intensities. It was suggested that the large amount of hydroxyl radicals formed at the initial stage played an essential role for the fast degradation of phenol during the first few minutes. Meanwhile, the interconversion between hydroxyl and sulfate radicals and their gradual consumption might account for the intensity decreases [42]. Therefore, by manipulating the concentration of C=O functional group, the tunable catalytic activity of carbon nanospheres was successfully realized.

To investigate the contribution of each reactive species and further validate the major reactive species responsible for phenol degradation, competitive radical tests using ethanol (EtOH) and *tert*-butyl alcohol (TBA) as radical scavengers were conducted. Both EtOH and TBA have the good scavenging effects against •OH with the reaction rate of $1.2 \times 10^9 - 2.8 \times 10^9\ M^{-1}s^{-1}$ and $3.8 \times 10^9 - 7.6 \times 10^9\ M^{-1}s^{-1}$, respectively [43]. For $SO_4^{\bullet-}$scavenging, due to the structure-bonded α-hydrogen atom, EtOH possesses a much higher scavenging capability than TBA ($1.6 \times 10^7 - 7.7 \times 10^7\ M^{-1}s^{-1}$ vs. $4.0 \times 10^5 - 8.1 \times 10^5\ M^{-1}\ s^{-1}$ [44]. Therefore, by addition of EtOH or TBA into the reaction solutions, not only the reactive species responsible for phenol degradation could be confirmed, but also the contribution of each reactive species to phenol degradation could be differentiated. Fig. 4(D) describes the results of the competitive radical tests. As seen, most of the catalytic reaction processes were suppressed after the addition of EtOH (0.2 M) and 95% of phenol was remained after the reaction, confirming •OH and $SO_4^{\bullet-}$ were the main reactive species responsible for phenol degradation. With the presence of TBA (0.2 M), less than 15% of phenol was decomposed at the end of 180 min. Compared with the catalytic reaction without the addition of scavengers, around 25% of initial phenol was destroyed by •OH, while 10% of initial phenol was destructed by $SO_4^{\bullet-}$.

To probe the insights of PMS activation on carbon spheres (CS), density functional theory (DFT) calculations were conducted. CS models with different oxygen-containing functional groups for PMS adsorption are displayed in Scheme 1. The adsorption energy (E_{ads}) of PMS on the CS was determined by $E_{ads} = E_{PMS+CS} - (E_{PMS} + E_{CS})$, where E_{PMS+CS} is the total energy of the CS with PMS adsorption, E_{PMS} and E_{CS} are the total energies of an isolated PMS molecule and the CS, respectively.

In the presence of —OH group on CS (Scheme 1 (a)), the PMS molecule was not attached on CS, and the corresponding E_{ads} is −3.04 eV, suggesting that activating PMS by —OH group was difficult, similar to the —OH group on N-doped SWCNTs [41]. When —OH group was replaced by —C=O group, $SO_4^{\bullet-}$radical could be generated directly. It was found the PMS molecule was dissociated into —OH and SO_4 groups spontaneously, and E_{ads} was calculated as −7.96 eV. The dissociated —OH group was then chemically bonded with the surface —C=O group to form —COOH group, which is in accordance with the variation of the oxygen-containing groups for the used CS-AIR catalyst. Then SO_4 group was released outside the system to form independent $SO_4^{\bullet-}$radical. Furthermore, the generation of $SO_4^{\bullet-}$was significantly affected by C=O group concentration. In the presence of three adjacent C=O groups (Scheme 1 (d)), PMS molecule would be attached on the C atom bonding with an O atom, which prevents the dissociation of PMS to form released $SO_4^{\bullet-}$. The calculation results also supported our previous studies that graphene oxide (GO) possessing a high oxygen content demonstrated much inferior PMS catalytic activity to rGO with a lower oxygen content. With the presence of —COOH group only, PMS was also dissociated into $-SO_4$ and —OH groups, which was similar to the case of —C=O group. However, the formed $-SO_4$ group favored to binding with a C atom in CS and the —OH group would bind with an H atom in —COOH group to form a H_2O molecule. Due to the strong interaction between $-SO_4$ and CS (E_{ads} of $-SO_4$ on CS is −6.98 eV), the release of SO_4 to produce $SO_4^{\bullet-}$radical is difficult. To conclude, —C=O at a low concentration could effectively activate PMS for dissociative generation of active $SO_4^{\bullet-}$radicals.

Fig. S7 (SI) demonstrates the phenol degradation profiles against the variation of initial phenol concentrations using the On^1–model of the catalyst (CS-AIR). A general trend can be observed that phenol degradation efficiency decreased with the increase of initial phenol concentration. When phenol concentration was increased to 60 ppm, only 20% phenol could be degraded at the end of 180 min of reaction time. This indicates that at the current PMS loading and catalyst dosage rates (2 g/L and 0.2 g/L, respectively), the amount of active species produced during the reaction was not high enough to provide proper degradation efficiency of phenol.

Phenol degradation experiments with different PMS loadings and catalyst dosages were further performed. The variation of PMS loading could exert a notable influence on catalytic phenol degradation efficiency (Fig. S8 (SI)). At 0.5 g/L PMS loading, less than 20% degradation of phenol could be achieved within 180 min. When PMS loading rate (1 g/L) was doubled, phenol degradation was enhanced from 20% to 35%, suggesting more reactive species were generated with the increase of PMS loading rate. Nevertheless, further increase of PMS loading rate to 4 g/L did not provide a significant improvement and 45% of phenol was decomposed at the end of reaction time, indicating that PMS was over-dosed and the limited amount of active sites on CS-AIR became the bottleneck for further enhancement of degradation efficiency.

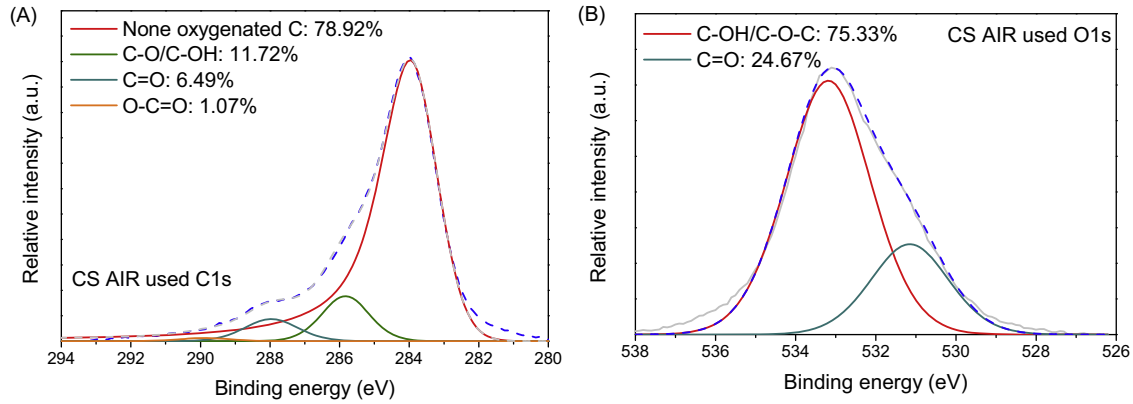

Fig. 5. (A) XPS survey on C1 s of used CS-AIR; (B) XPS survey on O1 s of used CS-AIR.

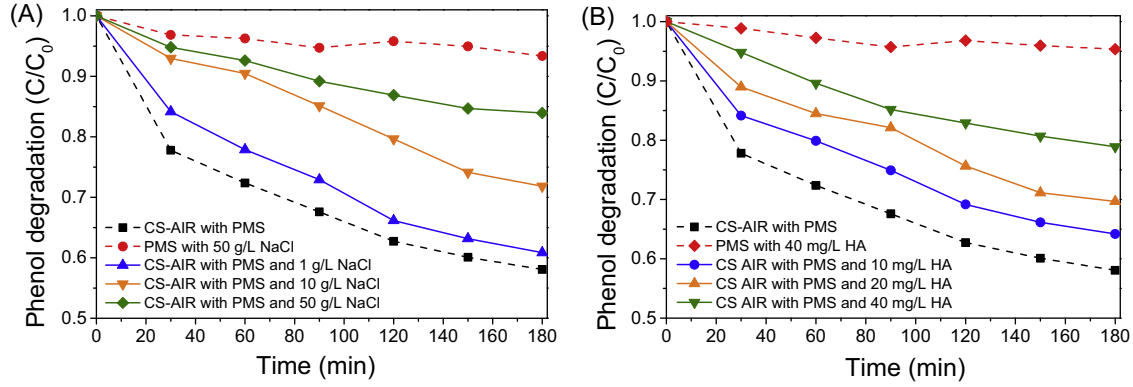

Fig. 6. (A) Effect of NaCl on catalytic phenol degradation; (B) effect of humic acid on catalytic phenol degradation. $[Phenol]_0$ = 20 mg/L; catalyst loading = 0.2 g/L; [PMS] = 2 g/L; temperature: 25 °C.

Fig. S9 (SI) describes the effect of catalyst dosage on phenol degradation. As seen, an increase of catalyst loading could lead to the improvement of degradation efficiency. Phenol removal rates at 0.1, 0.2 and 0.4 g/L of CS-AIR loading were 35%, 40% and 50%, respectively. It is worth noting, although higher catalyst loading provided more active sites, doubling or quadrupling the catalyst loading did not result in the remarkable elevation in degradation efficiency, which might be ascribed to the insufficient PMS loading.

The influence of reaction temperature on PMS activation for phenol degradation is presented in Fig. S10 (A) (SD). Phenol degradation efficiency slightly increased under the elevated temperature. When reaction temperature was elevated to 45 °C, 50% phenol removal was achieved at 3 h, while at reaction temperature of 35 and 25 °C, 45 and 40% of phenol degradation were obtained, respectively. Reaction activation energy was then evaluated according to the Arrhenius equation to be 83.2 kJ/mol (inset of Fig. S10 (A), much higher than the previously reported values of rGO (28.3 kJ/mol), nitrogen doped rGO (18.6 kJ/mol) and CNTs (33.3 kJ/mol) [26,36,42]. The high activation energy of carbon spheres suggested that compared with nanocarbon structures with multiple active sites, the surface functional groups on carbon spheres cannot effectively reduce the energy barrier for electron transfer, and thus demonstrated an inferior catalytic activity.

Stability and reusability tests employing CS-AIR (On^1–model) as the catalyst was also conducted (Fig. S10 (B), SD). The catalyst lost most of the activity from the second run, and only less than 20% of phenol was removed after 3 h. For the third run, catalyst was further deactivated and around 10% phenol was removed at the end of reaction. In order to investigate the deactivation mechanism, XPS survey was carried out to evaluate the changes of surface functional groups after the reaction. Fig. 5 (A) shows XPS survey of used CS-AIR on C 1 s region. Compared with corresponding XPS study on fresh CS-AIR, concentration of C=O functional group decreased from 8.71 to 6.39 at.% and the concentration of C—O/C—OH increased from 10.52 to 11.72 at.%, suggesting that some of the surface C=O groups were reduced to C—O/C—OH. While the percentage of O—C=O groups slightly increased due to the strong oxidative features of the produced reactive radicals. Moreover, DFT calculations revealed that the bonded hydroxyl group with C=O during the PMS activation process would also contribute to the increase of O—C=O group concentration. XPS survey on O1 s region of the used CS-AIR sample further consolidated the change in concentration of the surface functional groups (Fig. 5 (B)). After the catalytic reaction, the concentration of oxygen species C=O dropped dramatically from 48 to 24.7 at.%. Correspondingly, a sharp increase occurred to oxygen species C—O/C—OH from 52 to 75.3 at.%. Our previous study suggested that the adsorption of reaction intermediates and the oxidation of the functional groups might be the reasons for deactivation [27]. In this study, apart from the adsorption of reaction intermediates, it was proposed that the transformation from C=O to C—O/C—OH contributed to the catalytic activity loss in repeated use.

In real wastewater treatment, inorganic anions and natural organic matters (NOMs) widely exist at various concentrations. Some of the anions such as Cl^-, CO_3^{2-}, HPO_4^- and NO_3^- can quickly react with the generated reactive species and thus influence the catalytic reaction process. In practical processes, NaCl is extensively found at high concentrations (>50 g/L) from effluents of tannery and dye manufacturing and at lower concentrations from oil extraction wastewater [45]. Fig. 6(A) depicts the effect of NaCl on catalytic

oxidation of phenol. A general trend can be observed that addition of NaCl would suppress the catalytic degradation of phenol and a higher dosage of NaCl led to a greater suppression effect. Previous studies revealed that chloride anions would effectively scavenge $SO_4^{\bullet-}$ and $^{\bullet}OH$ (especially $SO_4^{\bullet-}$) to form secondary chlorine radicals such as $Cl^{\bullet}$, $Cl_2^{\bullet-}$ and $ClOH^{\bullet-}$, which possess much lower redox potentials than $SO_4^{\bullet-}$ and $^{\bullet}OH$ radicals and thus resulting in a lower efficiency [46]. On the other hand, the involvement of NOMs within the wastewater would lead to competitive reactions with the reactive species against the target pollutants and thus decrease their decomposition efficiency. Humic acid (HA) was then employed as the typical NOMs adding into the reaction solutions (Fig. 6(B)). As seen, PMS cannot be effectively activated by HA for phenol oxidation. In addition, phenol degradation decreased with the increase dosage of HA (from 10 to 40 mg/L). It was speculated that HA and its degradation intermediates not only compete against phenol for the generated reactive species consumption, but also block the active sites on the catalyst due to the strong π-π interaction [18].

4. Conclusion

In summary, elaborate catalyst design was conducted to deliver tailored amorphous carbon spheres for mimicking On-Off-On models of oxygen-containing functional groups. By ruling out the effects of sp^2 hybridized structure and defective sites, the contribution of the oxygen-containing functional groups, especially the C=O groups to the PMS activation was confirmed. Moreover, by affixation and removal of the oxygen-contained functional groups, the engineered catalysis on amorphous carbon spheres can be achieved. EPR spectrum and DFT calculations further consolidated the role of C=O groups in carbocatalytic PMS activation. Therefore, this study provides an in-depth insight to the nature of carbocatalysis.

Acknowledgements

This work was financially supported by Australian Research Council (DP130101319) and Science Foundation of China University of Petroleum, Beijing (No.2462016YJRC013). Computational study was supported by the National Computational Infrastructure (NCI) through the merit allocation scheme and used the NCI resources and facilities in Canberra, Australia.

Appendix A. Supplementary data

Supplementary data associated with this article can be found, in the online version, at http://dx.doi.org/10.1016/j.apcatb.2016.05.075.

References

[1] X. Hu, B. Liu, Y. Deng, H. Chen, S. Luo, C. Sun, P. Yang, S. Yang, Appl. Catal. B 107 (2011) 274–283.
[2] X. Wang, Y. Qin, L. Zhu, H. Tang, Environ. Sci. Technol. 49 (2015) 6855–6864.
[3] P. Gao, Z. Liu, M. Tai, D.D. Sun, W. Ng, Appl. Catal. B 138–139 (2013) 17–25.
[4] Y. Wang, H. Sun, H.M. Ang, M.O. Tadé, S. Wang, ACS Appl. Mater. Interfaces 6 (2014) 19914–19923.
[5] Y. Ren, L. Lin, J. Ma, J. Yang, J. Feng, Z. Fan, Appl. Catal. B 165 (2015) 572–578.
[6] V.J.P. Vilar, F.C. Moreira, A.C.C. Ferreira, M.A. Sousa, C. Gonçalves, M.F. Alpendurada, R.A.R. Boaventura, Water Res. 46 (2012) 4599–4613.
[7] L. Yang, C. Hu, Y. Nie, J. Qu, Appl. Catal. B 97 (2010) 340–346.
[8] L. Hu, X. Yang, S. Dang, Appl. Catal. B 102 (2011) 19–26.
[9] H. Hussain, I.R. Green, I. Ahmed, Chem. Rev. 113 (2013) 3329–3371.
[10] G.P. Anipsitakis, D.D. Dionysiou, Environ. Sci. Technol. 38 (2004) 3705–3712.
[11] S.K. Ling, S.B. Wang, Y.L. Peng, J. Hazard. Mater. 178 (2010) 385–389.
[12] G.P. Anipsitakis, D.D. Dionysiou, Environ. Sci. Technol. 37 (2003) 4790–4797.
[13] K.H. Chan, W. Chu, Water Res. 43 (2009) 2513–2521.
[14] E. Saputra, S. Muhammad, H.Q. Sun, H.M. Ang, M.O. Tade, S.B. Wang, Environ. Sci. Technol. 47 (2013) 5882–5887.
[15] Y. Wang, H. Sun, H.M. Ang, M.O. Tadé, S. Wang, Appl. Catal. B 164 (2015) 159–167.
[16] W. Zhang, H.L. Tay, S.S. Lim, Y. Wang, Z. Zhong, R. Xu, Appl. Catal. B 95 (2010) 93–99.
[17] Z. Huang, H. Bao, Y. Yao, W. Lu, W. Chen, Appl. Catal. B 154–155 (2014) 36–43.
[18] X. Duan, Z. Ao, L. Zhou, H. Sun, G. Wang, S. Wang, Appl. Catal. B 188 (2016) 98–105.
[19] S. Navalon, A. Dhakshinamoorthy, M. Alvaro, H. Garcia, Chem. Rev. 114 (2014) 6179–6212.
[20] H. Sun, G. Zhou, Y. Wang, A. Suvorova, S. Wang, ACS Appl. Mater. Interfaces 6 (2014) 16745–16754.
[21] L. Dai, Y. Xue, L. Qu, H.-J. Choi, J.-B. Baek, Chem. Rev. 115 (2015) 4823–4892.
[22] G. Dong, K. Zhao, L. Zhang, Chem. Commun. 48 (2012) 6178–6180.
[23] B. Frank, J. Zhang, R. Blume, R. Schlogl, D.S. Su, Angew. Chem. Int. Ed. 48 (2009) 6913–6917.
[24] X.-K. Kong, Z.-Y. Sun, M. Chen, C.-L. Chen, Q.-W. Chen, Energy Environ. Sci. 6 (2013) 3260–3266.
[25] H.Q. Sun, S.Z. Liu, G.L. Zhou, H.M. Ang, M.O. Tade, S.B. Wang, ACS Appl. Mater. Interfaces 4 (2012) 5466–5471.
[26] H. Sun, C. Kwan, A. Suvorova, H.M. Ang, M.O. Tadé, S. Wang, Appl. Catal. B 154–155 (2014) 134–141.
[27] H. Sun, Y. Wang, S. Liu, L. Ge, L. Wang, Z. Zhu, S. Wang, Chem. Commun. 49 (2013) 9914–9916.
[28] W.C. Peng, S.Z. Liu, H.Q. Sun, Y.J. Yao, L.J. Zhi, S.B. Wang, J. Mater. Chem. A 1 (2013) 5854–5859.
[29] M.M. Titirici, A. Thomas, M. Antonietti, Adv. Funct. Mater. 17 (2007) 1010–1018.
[30] B. Delley, J. Chem. Phys. 113 (2000) 7756–7764.
[31] F. Ortmann, F. Bechstedt, W.G. Schmidt, Phys. Rev. B: Condens. Matter 73 (2006) 205101.
[32] N. Shimodaira, A. Masui, J. Appl. Phys. 92 (2002) 902–909.
[33] X. Sun, Y. Li, Angew. Chem. Int. Ed. 43 (2004) 597–601.
[34] X. Sun, Y. Li, Langmuir 21 (2005) 6019–6024.
[35] X. Zhang, J. Ma, W. Yang, Z. Gao, J. Wang, Q. Liu, J. Liu, X. Jing, CrystEngComm 16 (2014) 4016–4022.
[36] H. Sun, S. Liu, G. Zhou, H.M. Ang, M.O. Tadé, S. Wang, ACS Appl. Mater. Interfaces 4 (2012) 5466–5471.
[37] B. Frank, R. Blume, A. Rinaldi, A. Trunschke, R. Schlogl, Angew. Chem. Int. Ed. 50 (2011) 10226–10230.
[38] D.E. Jiang, B.G. Sumpter, S. Dai, J. Chem. Phys. 126 (2007) 134701.
[39] G.-D. Fang, D.D. Dionysiou, S.R. Al-Abed, D.-M. Zhou, Appl. Catal., B 129 (2013) 325–332.
[40] Y. Zhou, J. Jiang, Y. Gao, J. Ma, S.-Y. Pang, J. Li, X.-T. Lu, L.-P. Yuan, Environ. Sci. Technol. 49 (2015) 12941–12950.
[41] X. Duan, Z. Ao, H. Sun, L. Zhou, G. Wang, S. Wang, Chem. Commun. 51 (2015) 15249–15252.
[42] X. Duan, Z. Ao, S. Sun, Y. Wang, J. Kang, F. Liang, Z.H. Zhu, S. Wang, ACS Appl. Mater. Interfaces 7 (2015) 4169–4178.
[43] G.V. Buxton, C.L. Greenstock, W.P. Helman, A.B. Ross, J. Phys. Chem. Ref. Data 17 (1988) 513–886.
[44] P. Neta, R.E. Huie, A.B. Ross, J. Phys. Chem. Ref. Data 17 (1988) 1027–1284.
[45] J. Vittenet, J. Rodriguez, E. Petit, D. Cot, J. Mendret, A. Galarneau, S. Brosillon, Microporous Mesoporous Mater. 189 (2014) 200–209.
[46] R. Yuan, S.N. Ramjaun, Z. Wang, J. Liu, J. Hazard. Mater. 196 (2011) 173–179.